

Chapter 9

Variable Viscosity Jets: Entrainment and Mixing Process

L. Voivenel, E. Varea, L. Danaila, B. Renou, and M. Cazalens

9.1 Introduction

The theory of Kolmogorov [13] premises that at infinitely large Reynolds numbers, the statistical properties of the small scales should be universally determined by ν and $\bar{\epsilon}$, the kinematic viscosity and the mean energy dissipation rate, respectively. Implicit to this theory is that viscosity, considered as one independent parameter of the flow, is a ‘small scale’ quantity and thus should not affect large scale mixing. This is one possible explanation for why most studies focus on homogeneous fluids (same density and viscosity), or on variable-density flows [2, 18]. Nonetheless, many flows deal with real fluids, for which both density and viscosity fluctuate in space and time.

One of the first studies devoted to effects of viscosity was that of Campbell and Turner [8]. In order to determine the composition of a magmatic layer, they studied the injection of a fluid in a more viscous one (whose kinematic viscosities are, respectively, ν_l and ν_h , subscripts ‘l’ and ‘h’ stand for ‘low’ and ‘high’, respectively), for several ratios $R_v = \frac{\nu_h}{\nu_l}$ spread from 1 to 400. Campbell and Turner [8] observed a very different behaviour for the two extreme cases. Indeed, mixing does not occur at all for the $R_v = 400$ case. This phenomenon is due to a competition between the destabilizing inertial forces and the stabilizing viscous ones at the interface. Thus, the study of Campbell and Turner highlights that the large scale mixing is in fact, greatly viscosity-dependent and that Variable-Viscosity-Flow (hereafter referred to as VVF) should be carefully studied. Indeed, this kind of

L. Voivenel (✉) • L. Danaila • E. Varea • B. Renou
CORIA-UMR 6614, Normandie Université, CNRS, INSA et Université de Rouen,
Avenue de l’Université, 76800 St Etienne du Rouvray, Rouen, France
e-mail: voivenel@coria.fr

M. Cazalens
SAFRAN R&T Center, Paris, France

flow is frequent in industrial applications. Differences in the morphology of the VVFs were acknowledged, e.g. [7], but generally for large values of R_v . Particular attention has been given to the instabilities born at the interface of two variable-viscosity fluids [9–11, 17, 20]. To cite one example, combustion processes involve fluids with different physical and chemical properties (e.g. fuel and oxidizer).

Numerous questions, however, remain without clear answers. Some of them are fundamental, such as those dealing with the rate of entrainment and the associated phenomenology [1], or the exact expression of the mean energy dissipation rate [14, 19] which appears to be of great importance for flame stabilization and quenching [16]. Hence, experimental, numerical and theoretical efforts are to be devoted to traditional aerodynamic configurations (gaseous flow and relatively high Reynolds number).

The present study aims at furthering our understanding of VVFs, with a particular view on the very near field and turbulence generation. The roadmap of the paper is as follows. Section 9.2 details the experimental facility, whereas in Sect. 9.3 the optical diagnostics are presented. The fourth and fifth sections aim at developing results on the dynamic and scalar fields in VVF versus CVF, based on the same momentum and Reynolds number, respectively. Finally some conclusions drawn for the present study are provided.

9.2 Experimental Set-Up

The effects of viscosity variations are quantified by comparing the following cases:

- Constant-Viscosity Flow (CVF), which is the baseline case. A nitrogen jet issues in a coflow of nitrogen. The viscosity ratio of the two fluids is $R_v = 1$.
- Variable Viscosity Flow (VVF). A propane jet issues in a coflow of nitrogen. The latter is 3.5 times more viscous than the propane, so that $R_v = 3.5$. The density ratio is very nearly equal to 1.

The comparison between the two cases is based on the *same initial condition*, i.e. the same initial jet momentum, therefore the same injection velocity which is $U_{inj} = 1.45$ m/s. To remove any ambiguity regarding the role of the Reynolds number, the comparison between CVF and VVF at the same initial Reynolds numbers will be done in Sect. 9.5.

The flow facility is a round jet of diameter $D = 30$ mm surrounded by a (slight) coflow. Jet and coflow are enclosed in order to get well-defined boundary conditions allowing future accurate comparison with numerical simulations, Fig. 9.1. The coflow diameter, $D_{cof} = 800$ mm, is sufficiently large to restrain the wall influence on the main jet while isolating it from the exterior environment.

The main jet issues from a contraction designed to ensure a *top-hat* velocity profile at the nozzle exit. To achieve this objective, the two key parameters to be chosen are:

Fig. 9.1 Sketch of the experimental facility. Nozzle, confinement and optical accesses

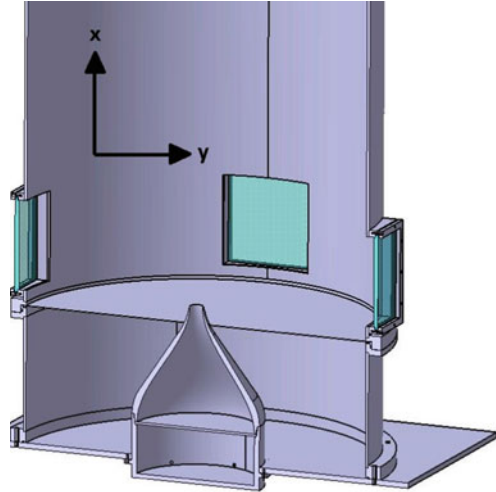
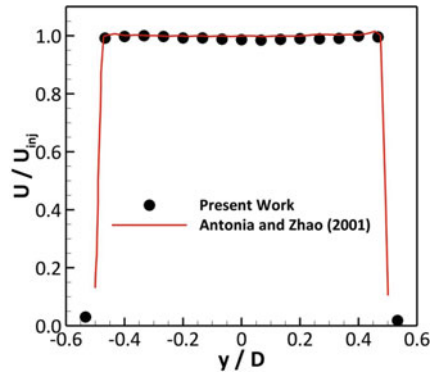


Fig. 9.2 Comparison of the velocity profile at the nozzle exit obtained in the current study and in Antonia and Zhao work



- the contraction ratio $C_R = \frac{D_{in}^2}{D_{out}^2}$, where D_{in} and D_{out} are the initial diameter of the contraction and the diameter at the contraction exit, respectively,
- the length on in-diameter ratio $\frac{L}{D_{in}}$, where L is the length of the contraction.

We have chosen to use the same values as Antonia and Zhao [3], i.e. $C_R = 87$ and $\frac{L}{D_{in}} \approx 1$. These parameters have then been used in the correlations provided by Bell and Mehta [4] to design contraction walls. The velocity profiles measured at the immediate vicinity of the nozzle exit by hot wire anemometry are consistent with those obtained by Antonia and Zhao [3], Fig.9.2. The initial turbulence intensity is 1 %.

The flow-rate is controlled by a Bronkhorst Coriolis Mass Flow Controller (model SNB13201070A/s) for the main jet and Bronkhorst Thermal Mass Flow Controller (model SNM4209650B) for the coflow. Both mass flow controllers have been calibrated or checked using an in-house calibration bench.

9.3 Optical Diagnostics

9.3.1 Velocity Measurements

Velocity field measurements were performed by stereo-Particle Image Velocimetry (stereo-PIV). The stereo-PIV technique has been chosen because of the three-dimensionality of velocity fluctuations. A Quantel Ultra Twin laser at 532 nm was used. A parallel laser sheet—passing through the jet center—is obtained using a cylindrical lens with a -40 mm focal length followed by a spherical lens of 500 mm focal length, Fig. 9.3. Seeding is done using Di-Ethyl-Hexyl-Sebacat (DEHS) particles whose size repartition is more homogeneous than that of vegetable oil (size order of magnitude around $1\ \mu\text{m}$), [6]. Two Imager ProX cameras (LaVision) with a pixel format of 2048×2048 pixels, coupled with two visible objectives Nikkor 105 mm and $f/2.8$, are placed on either side of the laser sheet at a 45° angle. A 60×60 mm field of view is recorded which corresponds to a magnification ratio of 35 pixels/mm. Each camera records particle images that are independently post-processed with the algorithm ‘Adaptive PIV’—provided by the Dantec software *Dynamic Studio* (3.4 release). Then, using a previously performed calibration, the n th 2D field from camera #1 is combined with the corresponding field from camera #2, creating a single 2 dimensions-3 components (2D-3C) velocity field.

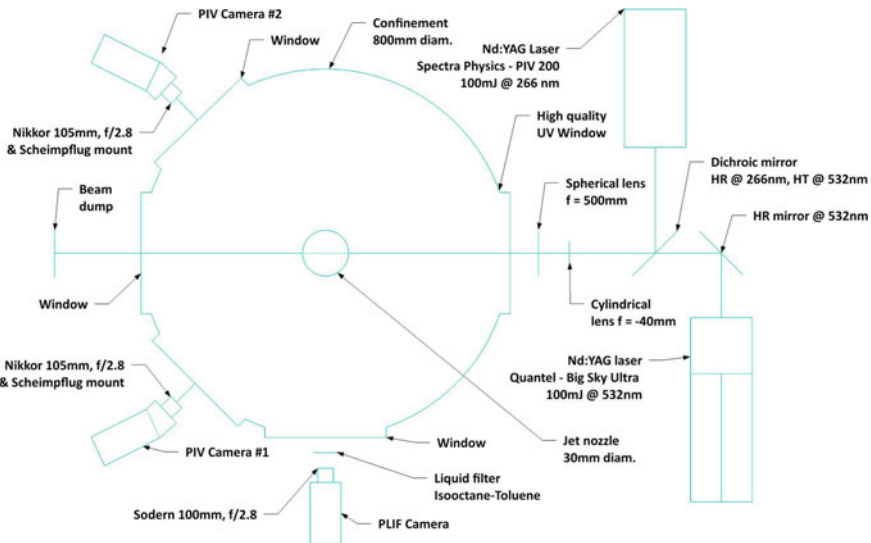


Fig. 9.3 Schematic diagram of the jet experiment

9.3.2 *Scalar Field Measurements*

Whilst the velocity field measurements are standard, the main experimental difficulty rests upon the scalar field measurements. Usually, acetone molecules are used as a tracer to perform Planar Laser Induced Fluorescence (PLIF) measurements. However, in order to obtain a sufficient signal-to-noise ratio, a great amount of tracer has to be used, leading to a modification of the seeded fluid properties. The focus of this work is on the effects of viscosity, therefore acetone is not the best choice here. Thus, an alternative molecule allowing a better signal-to-noise ratio while conserving the studied fluid properties was used. In addition to the previously discussed restrictions, the tracer must satisfy several other criteria:

- absorption wavelength has to be compatible with highly energetic laser at our disposal ($\lambda = 266$ nm),
- fluorescence spectrum must be shifted from the excitation wavelength
- evaporation properties must allow mixing with a gas.

The chosen tracer was anisole. To avoid ignition of the mixture when VVF cases are performed (propane is injected), the jet issues into nitrogen and not into an air coflow. Therefore, the strong quenching of anisole with O_2 is not an issue in our case. Moreover, the quantum yield, the ratio of photons absorbed to photons emitted through fluorescence, is very high which allows to inject a small quantity of anisole into the jet. The physical properties of the jet are therefore not altered.

To validate this technique, the linearity of the PLIF signal with the laser energy and the tracer concentration was tested. Another critical point is the proximity of the anisole absorption and emission bands. To eliminate the Mie signal at 266 nm coming from the DEHS particles as well as the stray light due to reflection at 266 nm, a liquid filter composed of iso-octane (spectroscopically neutral) and toluene as suggested in [15] was used. Indeed, the toluene absorbs predominantly at 266 nm and dimly from 270 nm, which is the beginning of the anisole fluorescence signal [5].

The tracer particles are excited using an Nd:YAG laser (Spectra Physics) with a fourth-harmonic generating crystal that produces a Q-switched laser output in the UV ($\lambda = 266$ nm, 100 mJ). A dichroic mirror is used to optically combine the PIV laser beam with LIF laser beam. The fluorescence signal is collected by an intensified CCD (ICCD) camera coupled to a UV Cerco 100 mm, f/2.8 lens. The ICCD camera is a Roper Scientific PIMAX 4 (16 bits) manufactured by Princeton Instruments with a pixel format of 1024×1024 pixels. The exposure time is set to 500 ns which is a compromise between fluorescence signal collection and the increase in noise level.

9.3.3 *Big Data*

With the emergence of new sensors for cameras, the recorded images can easily rise resolution of 5 Mega pixel. Moreover, the repetition rate is enhanced and a 5 Hz acquisition frequency is achieved. Therefore, a huge amount of data is accessible which makes it possible to obtain fully converged statistical results. However, the post-processing as well as the recording techniques needs to be designed and optimized in order to minimize the lag (during recording) and the overall post-processing time.

In the present study, a set of 3000 images is recorded for both the dynamic and the concentration fields. The issue concerning the acquisition is solved by using super-computers (Dell Z-800 Workstation) still affordable with enhanced access to memory (RAID 0). Two super-computers are used to record the dynamic field and the scalar fields.

As soon as the velocity field is concerned, two cameras of 5 M pixel each are used. Within 10 min of experiments, a set of two times 3000 images is stored on the hard drives which correspond to memory of approximately 94 Go. For the scalar field, the corresponding 3000 images are recorded using a Mega pixel camera which correspond to 12 Go of memory on the second workstation. Therefore, each data set represents a total amount of raw data of 108 Go. The question of classical storage of data on hard drives is addressed. To facilitate the access to the files, the data sets are uploaded on the Centre de Ressources Informatiques de Haute-Normandie (CRIHAN) storage servers where Tera bites of memory are available. Therefore, thanks to Giga bites ethernet connexion, an easy access to data is possible. In order to post-process the recorded data specific parallelized routines must be applied. This is facilitate since images are matrix and available toolbox in Matlab R2105 already exists. However, the post-processing time on a third workstation is around 1 week for both the scalar and the dynamic fields. A total amount of 92 Go of post-processed images is obtained. To optimize and decrease the calculation time, we are thinking on developing in-house post-processing routines which would be run on the CRIHAN servers where linux platform is in use. Therefore, storage and post-processing would be done on super-computer from the CRIHAN organization.

In the following sections, CVF and VVF cases will be compared on the basis of same jet momentum—Sect. 9.4—and same Reynolds number—Sect. 9.5—respectively.

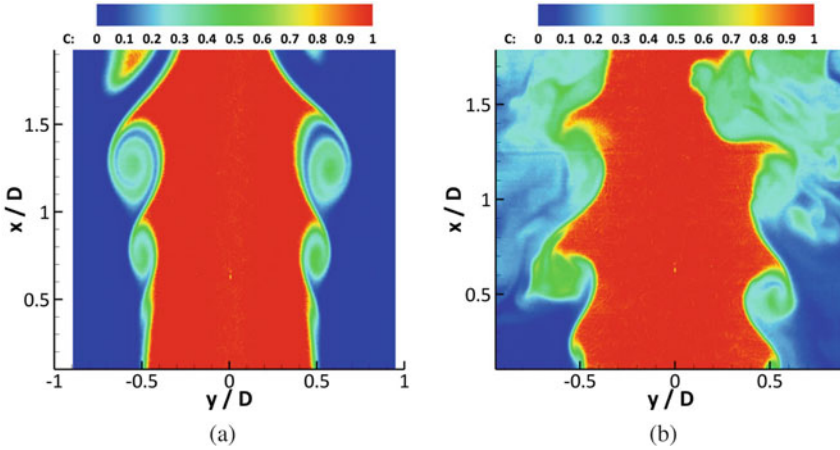


Fig. 9.4 Instantaneous images of mixing in N_2/N_2 jet and Propane/ N_2 jet. (a) CVF. (b) VVF

9.4 Comparison of CVF and VVF Based on the Same Initial Jet Momentum

9.4.1 Phenomenology

Figure 9.4 illustrates instantaneous images of the scalar distribution. Here C is the propane concentration—the mixture fraction—normalized such that $C = 1$ in the propane core jet and $C = 0$ in the N_2 coflow. A careful analysis of the scalar mixing provides a qualitative way to compare the two flows. Whilst the CVF exhibits classical Kelvin–Helmholtz vortices, Fig. 9.4a, the VVF, Fig. 9.4b, only provides a hint of the large scale, lateral engulfment of the ambient fluid, together with mixing at scales distributed over a much wider range.

Planar distributions of the mean and RMS (root mean squared) of the scalar are represented for the very near field of the flow, spanning between 0 and 2 jet diameters, in Fig. 9.5. Several observations may be made.

- The CVF potential core, Fig. 9.5a, image left-half-side, is wider than that of the VVF, Fig. 9.5a, image right-half-side, which suggests a better mixing for the latter. This statement is supported by the presence of propane in the full field of view for VVF. This is in contrast with the N_2/N_2 jet, where the core jet fluid (seeded N_2) is completely absent on the image edges.
- The largest RMS values are not located at the same axial locations: for the CVF flow, the largest values of the scalar RMS are located at $2D$, whereas for the VVF, the maxima are distributed much closer to the nozzle, between $0.5D - 1D$.

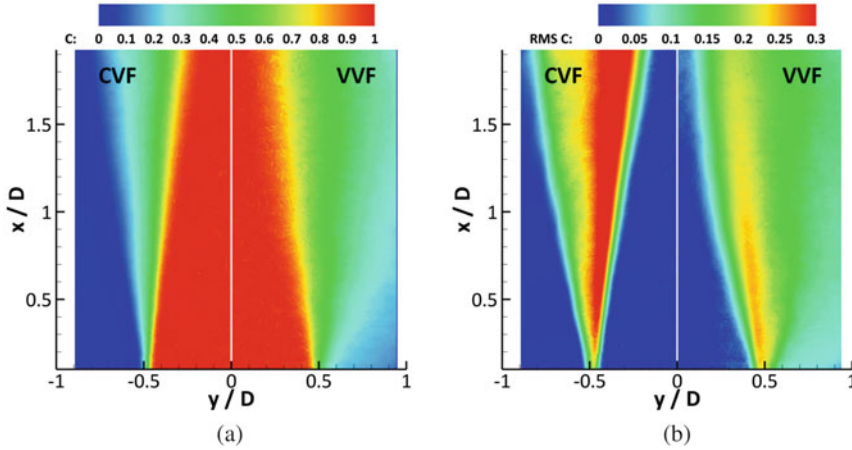


Fig. 9.5 Planar distributions of the (a) scalar mean and (b) RMS in CVF (N_2/N_2 jet), image *left-half-side*, and VVF (Propane/ N_2 jet), image *right-half-side*

The latter observation is to be understood in connection with the instantaneous images. The intense fluctuations are strongly correlated with the presence of the large structure—Kelvin–Helmholtz. For the VVF case, while at $y/D = 1$ engulfment only occurs, the mixing exhibits smaller and smaller scales at $y/D = 2$.

As far as the CVF is concerned, only large scale mixing occurs, thus explaining that larger fluctuations are observed, compared to the VVF case. This observation is strengthened by the study of the velocity field and more particularly of the mean lateral fluctuations (not shown here), whose evolution is similar to that of the scalar. Indeed, at a downstream position of one diameter, the lateral fluctuations are more intense in VVF than in CVF.

Moreover, there is a stronger decrease of the axial mean velocity in VVF, starting at the very early stage of injection, Fig. 9.6, indicating an increased entrainment of the ambient fluid into the jet fluid and an accelerated trend towards self-similarity.

Intense values of the axial velocity fluctuations, Fig. 9.7, as well as a faster trend towards isotropy (here quantified through the ratio $u_{\text{RMS}}/v_{\text{RMS}}$, Fig. 9.8, u and v being the axial and radial velocities, respectively) in VVF than in the baseline case (CVF) are observed.

9.4.2 Analysis

The birth of the turbulent fluctuations most likely results from a combination of four factors:

- (1) Kelvin–Helmholtz instabilities;
- (2) Wake instabilities behind the injector lip;

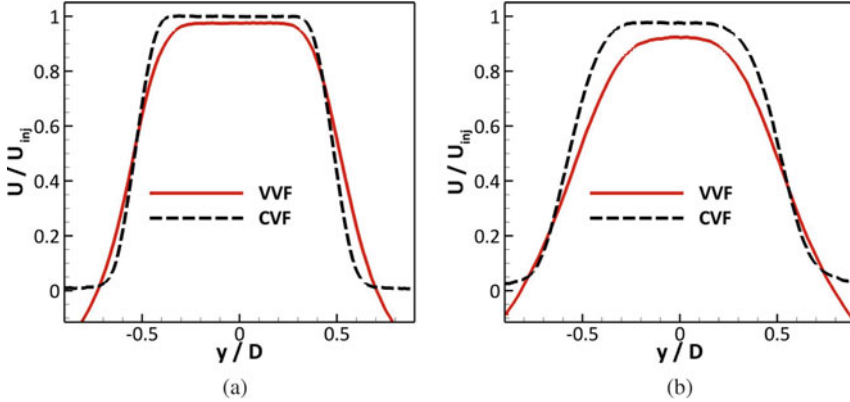


Fig. 9.6 Mean axial velocity normalized with respect to the injection velocity, for both CVF and VVF, at two axial locations: (a) $y = 1 D$ and (b) $y = 2 D$

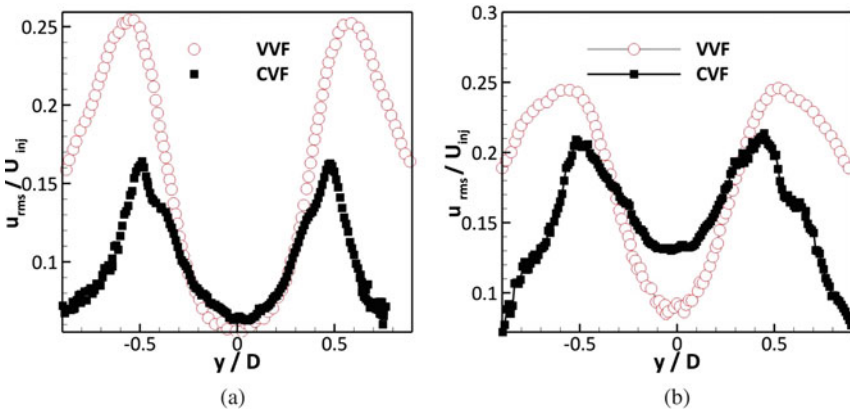


Fig. 9.7 Radial RMS normalized with respect to the injection velocity, for both CVF and VVF, at two axial locations: (a) $y = 1 D$ and (b) $y = 2 D$

- (3) Interface instabilities due to density gradients;
- (4) Interface instabilities due to viscosity jumps [12, 20].

Points (1) and (2) are characteristic of jet flows, constant-viscosity or not, thus, they cannot be responsible for such different behaviours. As far as the density effects are concerned, the studied configuration is that of a *heavy jet* (heavy fluid injected in a lighter one). Yet, according to Amielh et al. [2], density stratification for heavy jets results in mixing inhibition. The opposite is observed here, so the density effects are not responsible for the observed behaviour. Mixing enhancement is subdued to the occurrence of the four different types of instabilities at the jet edges.

Experimentally, the local viscosity is linked to the local concentration. A two species mixing law is applied. Hence, since the scalar field modifies the velocity

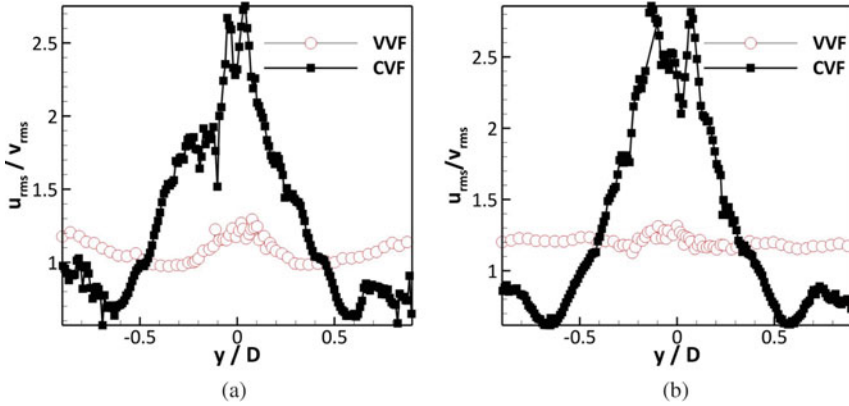


Fig. 9.8 Ratio $u_{\text{RMS}}/v_{\text{RMS}}$ for VVF and CVF, at two axial locations: (a) $y = 1 D$ and (b) $y = 2 D$

field—active scalar—both fields (dynamic and scalar) are coupled and must be studied together. By computing the joint probability function density (PDF) of the **mean** concentration and **mean** velocity, a complete mean flow mapping is obtained. Figure 9.9 reports the joint PDF of the mean concentration and mean axial velocity at 0.5 and 1.5 diameter, top and bottom, respectively. Right and left images correspond to the cases of CVF and VVF, respectively. To avoid ambiguity in the analysis, only statistics from the left part of the jet are presented. The two maxima located at $(\bar{C} = 1, \frac{\bar{U}}{U_{\text{inj}}} = 1)$ and $(\bar{C} = 0, \frac{\bar{U}}{U_{\text{inj}}} = 0)$ in Fig. 9.9a, c indicate a clear bimodal distribution for the CVF case. These two maxima are characteristic of the jet fluid and of the coflow, respectively. Thus, the lack of points between these two extremes confirms that the mixing is still at a very early stage in the N_2/N_2 jet.

In the propane case, at $y = 0.5 D$, Fig. 9.9b, the bimodal distribution is attenuated compared to the CVF case, Fig. 9.9a. Once again, this is consistent with the observation of a more advanced mixing in the VVF case. It is interesting to note that, if the maximum located at $(\bar{C} = 1, \frac{\bar{U}}{U_{\text{inj}}} = 1)$ is still present in the propane jet, it is not the case anymore for the second extremum $(\bar{C} = 0, \frac{\bar{U}}{U_{\text{inj}}} = 0)$. The former is shifted to a negative axial velocity $(\frac{\bar{U}}{U_{\text{inj}}} = -0.2)$ and a more important value of \bar{C} (e.g. $\bar{C} = 0.2$). These values can be explained by the presence of a recirculation zone which bring propane into the coflow.

The mean radial velocity and mean concentration joint PDF's allow us to highlight the processes at play—entrainment or jet expansion—at the considered downstream locations. Figure 9.10 shows the joint PDF of the mean concentration and mean radial velocity at 0.5 and 1.5 diameter, top and bottom, respectively. Right and left images correspond to the cases of CVF and VVF, respectively.

Looking at the CVF case, at $y = 0.5 D$, the existence of the bimodal distribution previously observed is confirmed, Fig. 9.10a. The few points $(\bar{C} = 0, \frac{\bar{V}}{U_{\text{inj}}} > 0)$ indicate the birth of the Kelvin–Helmholtz instabilities in the coflow. At downstream

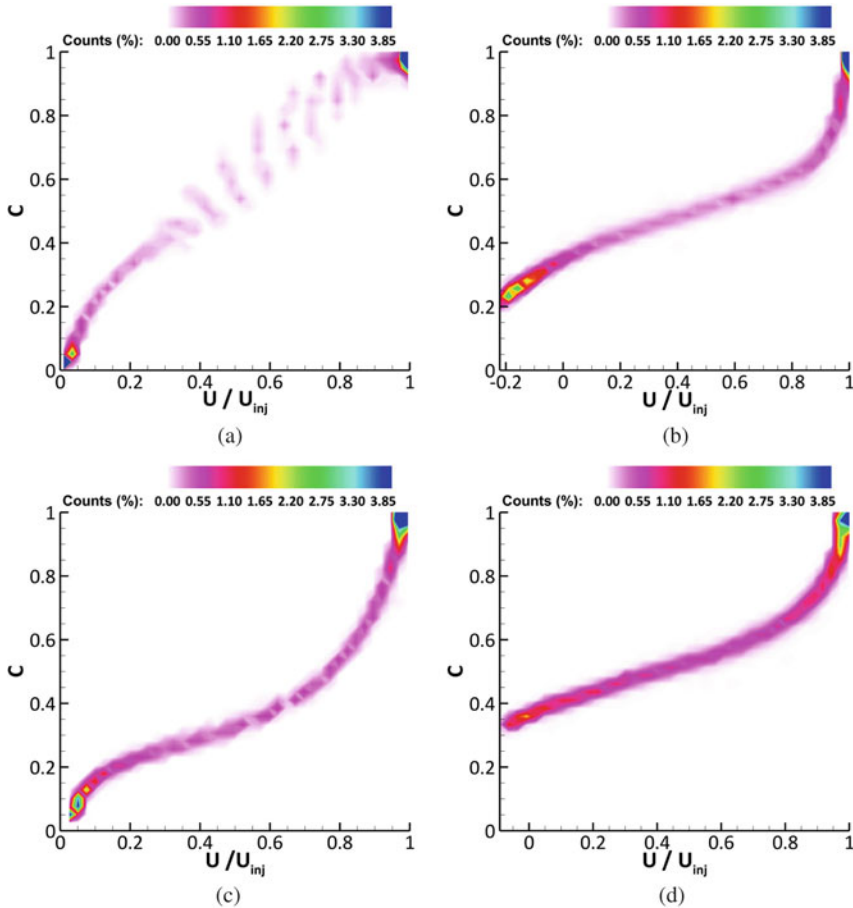


Fig. 9.9 Joint probability density functions of the mean concentration and mean axial velocity (\bar{C} , \bar{U}) for CVF (left) and VVF (right), at two axial locations: $y = 0.5 D$ (top) and $y = 1.5 D$ (bottom). (a) CVF at $y = 0.5 D$, (b) VVF at $y = 0.5 D$, (c) CVF at $y = 1.5 D$, (d) VVF at $y = 1.5 D$

location $y = 1.5 D$, the positive radial velocities are now associated with a lower concentration, $\bar{C} \approx 0.1$, Fig. 9.10c. This can be interpreted as the beginning of the large scale mixing—ensured by the Kelvin–Helmholtz instabilities—between jet and coflow. Moreover, the start of the jet expansion is observed through the points ($\bar{C} = 1$, $\frac{\bar{V}}{U_{inj}} < 0$).

The phenomenology identified for the VVF case is again very different from that observed in the N_2 jet. At $y = 0.5 D$, three particular zones may be distinguished, Fig. 9.10b. The first one, whose meaning is the most easily explained, is the maximum located at ($\bar{C} = 1$, $\frac{\bar{V}}{U_{inj}} = 0$). It corresponds to the jet core where the velocity vectors are only oriented along the axial direction. The second local

maximum displays the following characteristics: a mean concentration around 0.55 and a negative radial velocity, which can be interpreted as the jet expansion in a zone where the mixing with the host fluid is already at an advanced stage. Finally, the last remarkable area is characterized by a low mean concentration, $\bar{C} \approx 0.2$ —and a positive radial velocity. This combination indicates the presence of ambient fluid inflows—through the Kelvin–Helmholtz instabilities. This interpretation is confirmed by the disappearance of the points ($\bar{C} \approx 0.2$, $\frac{\bar{V}}{U_{inj}} < 0$) at the location $y = 1.5 D$, where the large scale structures are no longer visible on the instantaneous images, Fig. 9.10d. It can also be noticed that the total number of points corresponding to the jet core has been divided by 1.5. Apart from this zone, the other points have a negative radial velocity, indicating that the main phenomenon at this location is the jet expansion.

From the results and analysis presented above, it can be concluded that clear experimental evidence has been obtained to claim that viscosity stratification has an important influence on turbulence, for viscosity ratios as low as 3.5.

9.5 Comparison of VVF and CVF Based on the Same Reynolds Number

In the previous section, CVF and VVF cases for the same jet momentum were compared. It can be argued that the Reynolds number in the N_2 jet is 3.5 times lower than propane jet, thus explaining the observed discrepancies. To address this, measurements were taken in the CVF case with the same Reynolds number as in the VVF case, i.e. with an injection velocity $U_{inj} = 4.37$ m/s.

Figure 9.11a, b show instantaneous scalar distribution in CVF and VVF, respectively. Once again, the topology of the two cases is completely different. If the CVF case is indeed more turbulent than in the previous experiments, Fig. 9.4, it still does not present the large range of scales exhibited by the VVF.

The map of the scalar mean is presented in Fig. 9.12a. It is observed that a shift occurs in the virtual origin of the N_2/N_2 jet, compared to the constant-viscosity case detailed in the previous section. As far as the jet angle is concerned, it is smaller in the CVF case than in the VVF case, indicating a less advanced mixing.

The maxima of the RMS of the longitudinal fluctuations are once again correlated with the presence of large structures. This is particularly visible when attention is focused on the top of the image in Fig. 9.12b (from $y = 1.2 D$ up to $y = 1.9 D$). Indeed, this is the largest zone of intense fluctuations. Confronting with the instantaneous image, Fig. 9.11a, it also corresponds to the location of the largest structures. Thus, even if the CVF topology differs slightly from that of the previous section (Sect. 9.4, same jet momentum), up to this point the observations previously made still hold.

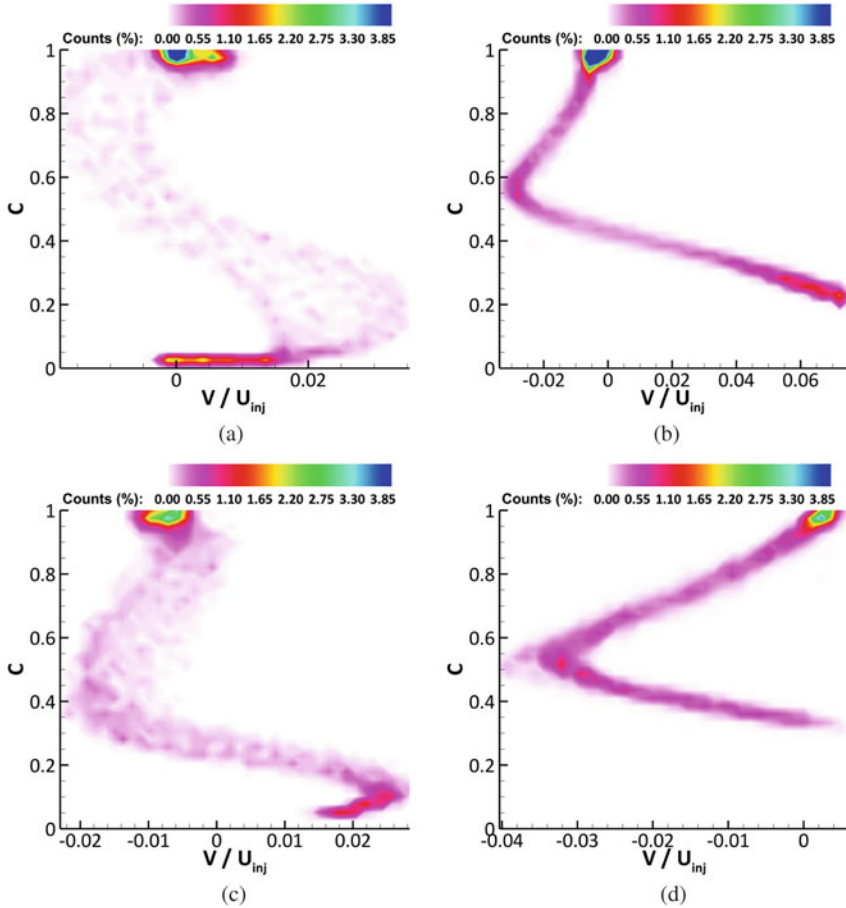


Fig. 9.10 Joint probability density functions of the mean concentration and mean radial velocity (\bar{C} , $\frac{\bar{v}}{U_{inj}}$) for CVF (left) and VVF (right), at two axial locations: $y = 0.5 D$ (top) and $y = 1.5 D$ (bottom). (a) CVF at $y = 0.5 D$, (b) VVF at $y = 0.5 D$, (c) CVF at $y = 1.5 D$, (d) VVF at $y = 1.5 D$

Profiles of mean axial velocity are reported in Fig. 9.13. For a given axial location, they present a more advanced decrease in the variable-viscosity case than in the N_2/N_2 jet. Similarly, Fig. 9.14 shows the longitudinal fluctuations are stronger in the VVF case and seem to have started their decrease contrary to those in the CVF which still increase with the axial location.

To conclude, this section illustrates that the discrepancies are still present, even if a little less pronounced, when comparing VVF and CVF configurations with the same Reynolds number (i.e. different injection velocities).

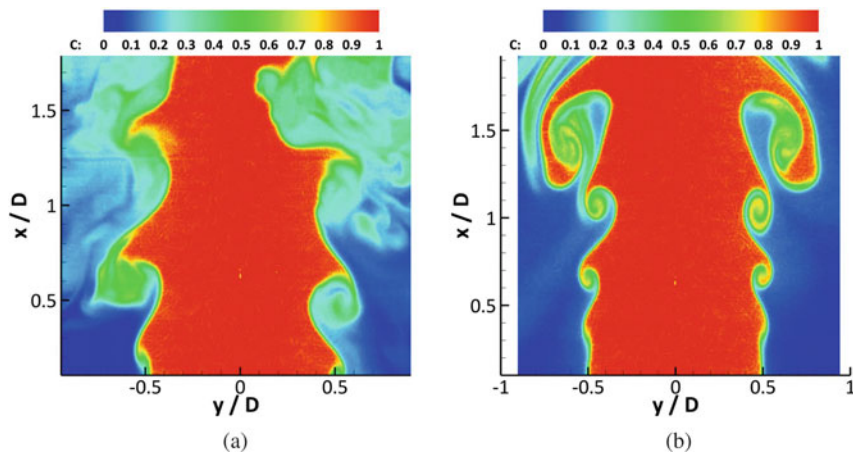


Fig. 9.11 Instantaneous images of mixing in N_2/N_2 jet and variable-viscosity (Propane/ N_2) jet. (a) CVF. (b) VVF

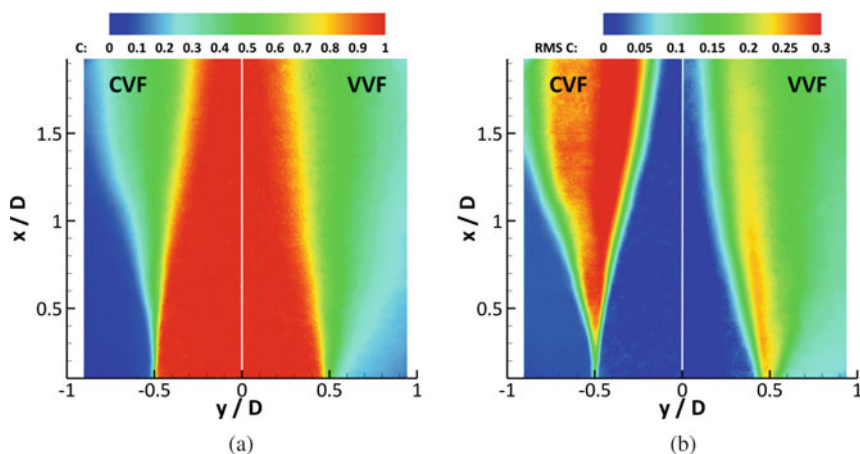


Fig. 9.12 Planar distributions of the (a) scalar mean and (b) RMS in CVF (N_2/N_2 jet), image left-half-side, and VVF (Propane/ N_2 jet), image right-half-side

9.6 Conclusion

With respect to the classical constant-viscosity jet, the variable-viscosity jet of a fluid issuing into a more viscous ambient fluid exhibits in the very near field:

- enhanced entrainment
- more important turbulent fluctuations.

We explain these phenomena by stating that if the different ‘steps’ of the turbulence are the same by nature (birth, growth, decrease and death), their duration is shorter

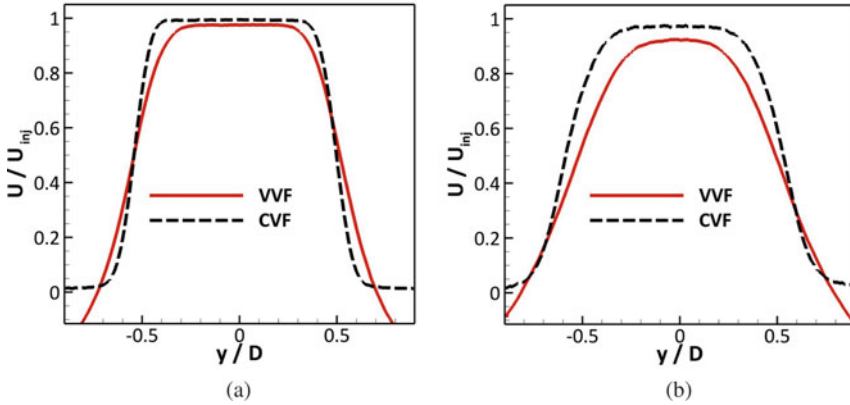


Fig. 9.13 Mean axial velocity normalized with respect to the injection velocity, for both CVF and VVF, at two axial locations: (a) $y = 1 D$ and (b) $y = 2 D$

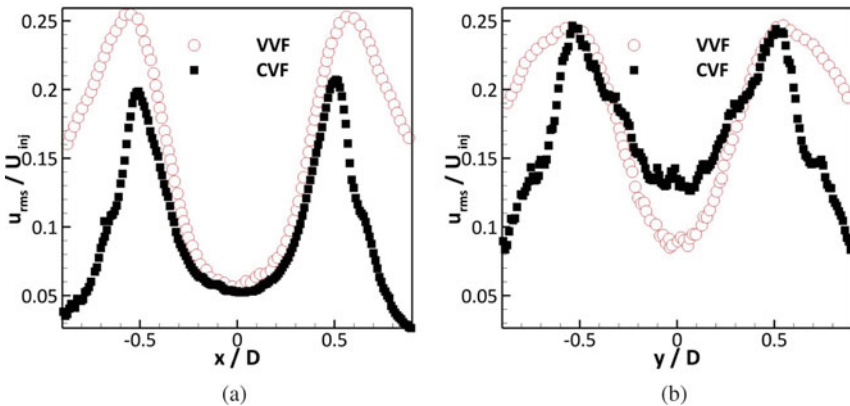


Fig. 9.14 Radial RMS normalized with respect to the injection velocity, for both CVF and VVF, at two axial locations: (a) $y = 1 D$ and (b) $y = 2 D$

in VVF than in CVF. Moreover, processes like fluctuation production are more intense in flow with variable viscosities. It means that, even when viscosity gradients disappear (far from the injection where the mixing is achieved), they have already significantly modified the flow dynamics. Thus, its final state will be different from a flow which has not be subjected to viscosity effects, even if their initial conditions— Re or jet momentum—are identical. The general message of this contribution is that whereas the viscosity itself indeed acts at the level of smallest scales, flows with viscosity variations at a large scale (such as jets issuing in different environment) are characterized by effects of viscosity variations at any scale, including the largest. A simple visualization of the scalar dispersion allows us to observe a significant disparity between VVF and CVF behaviours, leading us to state that the viscosity affects the topology and the dynamics of the whole flow at all scales.

Acknowledgements Financial support from the French National Research Agency under the project ‘MUVAR’ is gratefully acknowledged. We thank Dr. G. Godard, A. Vandel and C. Gobin for their helpful assistance in the experimental set-up. The authors thank H. Cavalier for his expertise in safety procedures concerning flammable mixtures. A first version of the paper was presented at the 10th Pacific Symposium in Flow Visualization and Image Processing, Naples 15–18 June 2015 as paper 240.

References

1. G.N. Abramovich, *The Theory of Turbulent Jets* (The MIT Press, Cambridge, 1963)
2. M. Amielh, T. Djeridane, F. Anselmet, L. Fulachier, Velocity near-field of variable density turbulent jets. *Int. J. Heat Mass Transf.* **39**, 2149–2164 (1996)
3. R.A. Antonia, Q. Zhao, Effects of initial conditions on a circular jet. *Exp. Fluids* **31**, 319–323 (2001)
4. J.H. Bell, R.D. Mehta, Contraction design for small low-speed wind tunnel. *TR* **84**, 1–37 (1988)
5. I. Berلمان, *Handbook of Fluorescence Spectra of Aromatic Molecules*, 2nd edn. (Academic, New York, 1971)
6. G. Boutin, Mélange et micro-mélange dans un réacteur à multiples jets cisailés. Ph.D. thesis, Université de Rouen, 2010
7. R. Cabra, J.Y. Chen, R.W. Dibble, A.N. Karpetsis, R.S. Barlow, Lifted methane-air jet flame in vitiated co-flow. *Combust. Flame* **143**(4), 491–506 (2005)
8. I.H. Campbell, J.S. Turner, The influence of viscosity on fountains in magma chamber. *J. Petrol.* **27**, 1–30 (1986)
9. R. Govindarajan, Effect of miscibility on the linear instability of two-fluid channel flow. *Int. J. Multiphase Flow* **30**, 1177–1192 (2004)
10. R. Govindarajan, K. Sahu, Instabilities in viscosity-stratified flow. *Ann. Rev. Fluid Mech.* **46**, 331–353 (2014)
11. R. Govindarajan, V. L'vov, I. Procaccia, Retardation of the onset of turbulence by minor viscosity contrasts. *Phys. Rev. L* **87**, 174501 (2001)
12. A. Harang, O. Thual, P. Brancher, T. Bonometti, Kelvin-helmholtz instability in the presence of variable viscosity for mudflow resuspension in estuaries. *Environ. Fluid Mech.* **14**, 743–769 (2014)
13. A.N. Kolmogorov, The local structure of turbulence in incompressible viscous fluids for very large Reynolds numbers. *Dokl. Akad. Nauk SSSR* **30**(4), 301–305 (1941)
14. K. Lee, S. Girimaji, J. Kerimo, Validity of Taylor's dissipation-viscosity independence postulate in variable-viscosity turbulent fluid mixtures. *Phys. Rev. Lett.* **101**(7), 074501 (2008)
15. N. Pasquier, B. Lecordier, A. Cessou, Investigation of flame propagation through a stratified mixture by simultaneous piv/lif measurements, in *Proceedings of the Combustion Institute* (2007)
16. N. Peters, F. Williams, Lift-off characteristics of turbulent jet diffusion flames. *AIAA J.* **21**, 3 (1983)
17. A. Pinarbasi, A. Liakopoulos, The effect of variable viscosity on the interfacial stability of two-layer Poiseuille flow. *Phys. Fluids* **7**(6), 1318–1324 (1995)
18. W.M. Pitts, Effects of global density ratio on the centerline mixing behavior of axisymmetric turbulent jets. *Exp. Fluids* **11**, 125–134 (1991)
19. B. Talbot, L. Danaila, B. Renou, Variable-viscosity mixing in the very near field of a round jet. *Phys. Scr.* **T155**, 014006 (2013)
20. C.S. Yih, Instability due to viscosity stratification. *J. Fluids Mech.* **27**(2), 337–352 (1967)